

High-rate, high-fidelity entanglement of qubits across an elementary quantum network

L. J. Stephenson,* D. P. Nadlinger,* B. C. Nichol, S. An, P. Drmota,
 T. G. Ballance,[†] K. Thirumalai, J. F. Goodwin, D. M. Lucas, and C. J. Ballance[‡]
Department of Physics, University of Oxford, Clarendon Laboratory, Parks Road, Oxford OX1 3PU, U.K.

We demonstrate remote entanglement of trapped-ion qubits via a quantum-optical fiber link with fidelity and rate approaching those of local operations. Two $^{88}\text{Sr}^+$ qubits are entangled via the polarization degree of freedom of two photons which are coupled by high-numerical-aperture lenses into single-mode optical fibers and interfere on a beamsplitter. A novel geometry allows high-efficiency photon collection while maintaining unit fidelity for ion-photon entanglement. We generate remote Bell pairs with fidelity $F = 0.940(5)$ at an average rate 182s^{-1} (success probability 2.18×10^{-4}).

The ability to form logical connections between all quantum bits (qubits) of a quantum processor is a prerequisite for building a fault-tolerant universal device [1]. Trapped atomic ions have been identified as an excellent candidate qubit technology because they allow the implementation of high-fidelity single-qubit operations [2, 3], two-qubit phonon-mediated gates [3, 4] and quantum memories [5, 6] with high fidelity. However, the number of ions that can be reliably interfaced in a single trap is limited by the motional mode density, necessitating architectures with multiple trap zones each hosting comparatively few ions. Trap zones can be interfaced by physically shuttling qubits across centimeter-scale distances using electric fields [7], or by using photons to distribute entanglement over larger distances [8]. Photonic entanglement could also increase the connectivity of trapped-ion qubits via dynamically-switchable fiber links [9], or allow the interfacing of different qubit platforms [10]. It also enables other quantum networking applications such as quantum key distribution, teleportation of quantum states, and ‘blind’ quantum computing [11, 12]. For ions, the entanglement rate is limited fundamentally by only the photon scattering rate ($\sim 100\text{ MHz}$), exceeding local multi-qubit operation rates (motional gates [13] and shuttling [14, 15]) at $\sim 1\text{ MHz}$ secular trap frequencies. In practice, photonic entanglement rates have been far lower than this, limited principally by low photon collection efficiencies [16]; the highest previously reported rate for ions was 4.5s^{-1} [17]. In neutral atoms and nitrogen vacancy centers, $\sim 30\text{s}^{-1}$ were reached [18, 19]; faster ($\sim \text{kHz}$) rates have been achieved with quantum dot systems, with $\sim 60\%$ fidelity [20, 21]. Remote entanglement fidelities above 90% have not been reported for any physical systems with better than $\sim \text{mHz}$ rates [22, 23].

In this manuscript, we report the generation of entanglement between remote qubits at rates and fidelities approaching those of typical local operations, by swapping entanglement between photons emitted by the ions onto the ions themselves [24]. At these higher rates and fidelities, distillation procedures based on photonic entanglement [25] start to become a viable method for creating

high quality entanglement across a scalable trapped ion quantum computer.

A novel excitation scheme using $^{88}\text{Sr}^+$ ions with photon collection perpendicular to the static applied magnetic field allows an increased rate over previous experiments [17], with polarization mixing maximally suppressed by coupling into a single mode optical fiber. In contrast to previous schemes using $^{171}\text{Yb}^+$, the collection geometry does not impede the use of beams parallel to the applied magnetic field. This allows standard σ -polarized optical pumping to be employed, thus permitting the straightforward initialization of multiple ion species in a single trap.

We collect photons from the spontaneous decay of the excited electronic state $|5p\text{ }P_{1/2}, m=+1/2\rangle$ of $^{88}\text{Sr}^+$, as shown in Fig. 1a. Decays to the two states of the ground level $5s\text{ }S_{1/2}$ are associated with π and σ^+ polarized photons, forming an entangled ion-photon state given by

$$|\psi\rangle = \sqrt{\frac{2}{3}} |\downarrow\rangle |\sigma^+\rangle + \sqrt{\frac{1}{3}} |\uparrow\rangle |\pi\rangle ,$$

where the weightings are due to the Clebsch-Gordan coefficients for each decay path, and the ion qubit states are labeled with $|\downarrow\rangle$ and $|\uparrow\rangle$. Perpendicular to the magnetic field axis, the emitted field from the π decay has twice the intensity, and so for photons on the collection axis the ion-photon state is

$$|\psi\rangle = \frac{1}{\sqrt{2}} (|\downarrow\rangle |\text{H}\rangle + |\uparrow\rangle |\text{V}\rangle) , \quad (1)$$

where σ^+ and π have been relabeled H and V to emphasize that the two photon polarizations are both linear and orthogonal; note that this is a maximally-entangled Bell state.

The non-orthogonality of the σ^+ and π emissions away from the collection axis would normally reduce the fidelity of the ion-photon entanglement at the high numerical apertures needed to maximize the photon collection efficiency [26]. However, with the chosen collection geometry, coupling into a single mode optical fiber rejects the non-orthogonal component of the σ^+ emission, reducing the maximum possible collection efficiency but maintaining unit ion-photon Bell state fidelity independent of collection aperture (see Fig. 1b). In contrast to

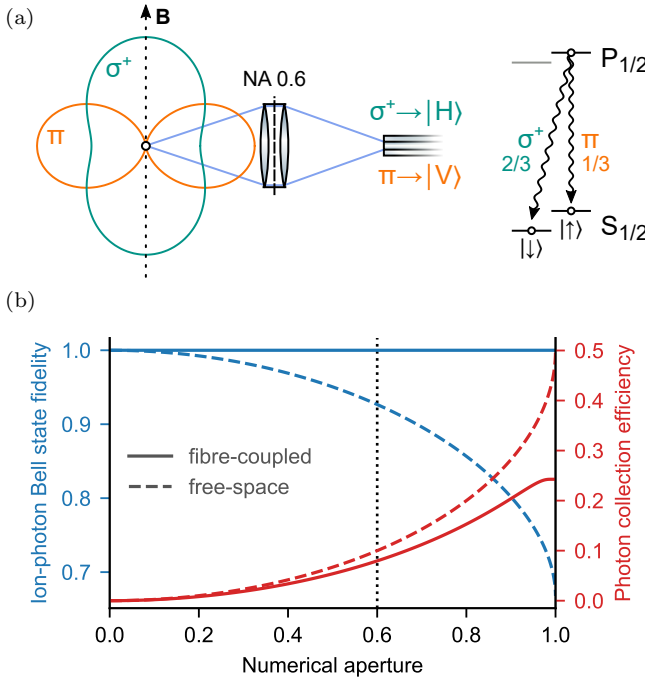


FIG. 1. (a) Intensity distribution of the light field for σ^+ and π decay channels, relative to the quantization axis set by the static magnetic field \mathbf{B} , and the branching fractions for each decay due to atomic selection rules. At the fiber input face, photons from σ^+ (π) decay map to the H (V) fiber polarization mode. (b) Maximum fraction of photons emitted by the ion that can be collected (red) and theoretical ion-photon entanglement fidelity (blue) versus collection optic numerical aperture. For free-space collection (dashed lines) polarization mixing leads to a loss in fidelity with increasing numerical aperture. To model the fiber-coupling (solid lines), we calculate the overlap of the light field with a Gaussian mode on the dashed plane in (a): a smaller fraction of the emission is collected, but the polarization mixing is completely suppressed. The vertical dashed line shows the NA 0.6 used in this work, where the fiber collection efficiency is 80 % of that in free-space.

other schemes, no photons of comparable wavelength are produced from undesired decay channels. These photons would otherwise have to be filtered [27], enabling higher rates to be achieved with our collection geometry and excitation scheme.

By collecting two such photons entangled with separated ions and erasing the which-path information from the photons, a projective measurement of the two-photon state in the Bell basis will herald the projection of the two ions into a corresponding Bell state [28].

In our experiment, $^{88}\text{Sr}^+$ ions are trapped in two identical, high-optical-access, microfabricated surface traps [29] in separate vacuum systems, designated “Alice” and “Bob”. In each system, a high-numerical-aperture (NA 0.6) lens, aligned perpendicular to the applied magnetic field of 0.56 mT, couples single photons

from the ion into an anti-reflection (AR) coated single-mode optical fiber. A second objective (NA 0.3) images the ion through a slot in the trap onto a photomultiplier tube to detect fluorescence from the ion.

The relevant electronic structure of $^{88}\text{Sr}^+$ is shown in Fig. 2. Ions are Doppler cooled with lasers at 422 nm and 1092 nm. The Zeeman structure of the ground level is used to encode the “Zeeman” qubit: $|S_{1/2}, m=-1/2\rangle =: |\downarrow\rangle$ and $|S_{1/2}, m=+1/2\rangle =: |\uparrow\rangle$. We also define an “optical” qubit between the metastable level $|4d D_{5/2}, m=-3/2\rangle =: |D\rangle$ and $|\downarrow\rangle$, using a narrow linewidth laser at 674 nm to coherently transfer population between either of the Zeeman qubit states and $|D\rangle$. As $|D\rangle$ is outside the Doppler cooling cycle, it can also be used to shelve population from $|\uparrow\rangle$ to measure the ground state qubit by fluorescence detection.

The experimental sequence for generating entangled photons is shown in Fig. 2. An optimized attempt section at rate 1 MHz, lasting at most 500 μs , is interleaved with 100 μs of Doppler cooling, until detection of an appropriate two-photon coincidence heralds the creation of ion-ion entanglement. (In single-ion/photon experiments, a single click of a chosen detector instead breaks this attempt loop and triggers the start of the analysis sequence.) The experimental sequence is controlled by an FPGA [30], incorporating the custom-optimized, pre-compiled section with decision branching in hardware, and just-in-time compiled sequences for qubit manipulations.

The projective measurement of the photons is performed with a partial Bell state analyzer, consisting of a 50:50 non-polarizing beamsplitter (NPBS) and polarizing beamsplitters (PBSs) on each output arm. All four output channels are monitored by avalanche photodiodes [31] (APDs), as shown in Fig. 3. Spatial mode matching of the photons from each system at the 50:50 beamsplitter is aided by recoupling the light into AR coated single-mode optical fibers before the APDs (coupling efficiency $\approx 90\%$). The total click efficiency into all APDs is typically 2.0 % and 2.4 % for Alice and Bob, respectively.

We first characterize the entanglement between the ion and emitted photon for each of the trap systems, using one detector in the apparatus shown in Fig. 3. We perform full tomography of the combined ion-photon state by independently rotating each qubit. Rotations of the ion state are performed on the optical qubit using the 674 nm laser after mapping $|\uparrow\rangle$ to $|D\rangle$ with a π -pulse. An over-complete set of ion and photon measurements is used to characterize the entangled ion-photon state, and calculate the maximum-likelihood estimate (MLE) of the composite density matrix. Rotations of the photon state are performed using the waveplates on the Bell state analyzer. The density matrices obtained indicate a fidelity of 97.90(12) % (97.70(12) %) with the maximally-entangled state, at an average rate of $4.0 \times 10^3 \text{ s}^{-1}$ ($5.7 \times 10^3 \text{ s}^{-1}$) for the Alice (Bob) system.

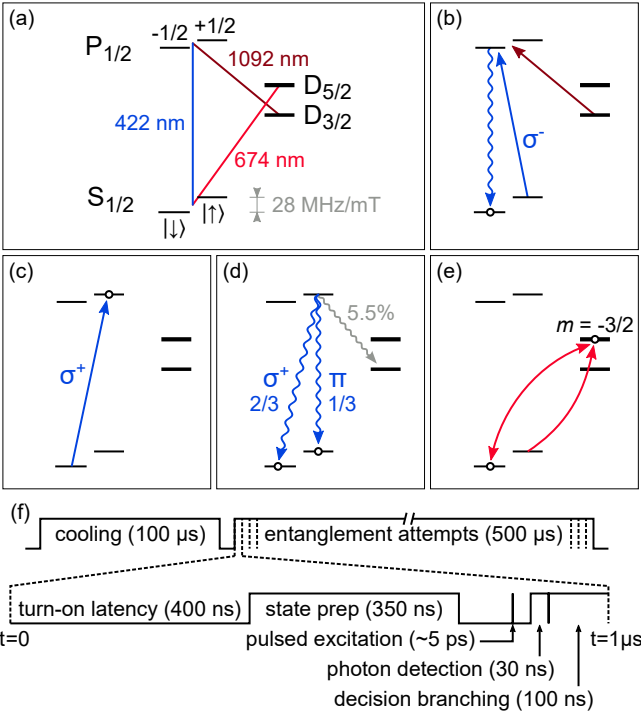


FIG. 2. (a) $^{88}\text{Sr}^+$ level diagram (not to scale). (b) The initial state preparation consists of optical pumping on the 422 nm transition, with a repumper at 1092 nm to clear the $D_{3/2}$ level. (c) A single ~ 5 ps pulse from a frequency-doubled mode-locked Ti:Sapphire laser coherently transfers the population to $P_{1/2}$, $m=+1/2$ with $\approx 95\%$ probability. (d) The ion decays to a superposition of $|\downarrow\rangle$ and $|\uparrow\rangle$, emitting a photon whose polarization state is entangled with the state of the ion. Decays to the $D_{3/2}$ manifold occur with probability 5.5 %, but as the 1092 nm photons are not transmitted by the fiber, the only effect is to lower the overall rate. (e) Qubit manipulations are performed on the 674 nm transition to $|D\rangle$ in order to analyze the final ion qubit state. (f) Experimental sequence: the ions are Doppler cooled for 100 μs before the attempt loop (lasting up to 500 μs) begins. The zoom view shows a single attempt, with latency ~ 400 ns between state preparation turn-on signal (at the very start of the sequence) and light arriving at the ion. State preparation (~ 350 ns) is followed by a 100 ns delay to ensure that the beams are fully extinguished before the pulsed excitation. The 30 ns photon detection window begins 30 ns after the excitation pulse to allow for detector latency. A further 100 ns at the end of the sequence is required for decision making in the event that a heralded pattern is detected.

Ion qubit rotation errors account for $\approx 0.6\%$ of the total error, at $\approx 0.3\%$ per rotation. We measure correlations of ion state with photon polarization of $P(|\uparrow\rangle|\text{V}) \approx P(|\downarrow\rangle|\text{H}) \approx 0.995$, which includes the error from one π -pulse on the ion qubit. This bounds the error due to all polarization mixing effects to $\lesssim 0.2\%$. Excited state preparation errors (preparing $|P_{1/2}, m=-1/2\rangle$ instead of $|P_{1/2}, m=+1/2\rangle$) depend on the polarization impurity of both the optical pumping and pulsed excitation beams

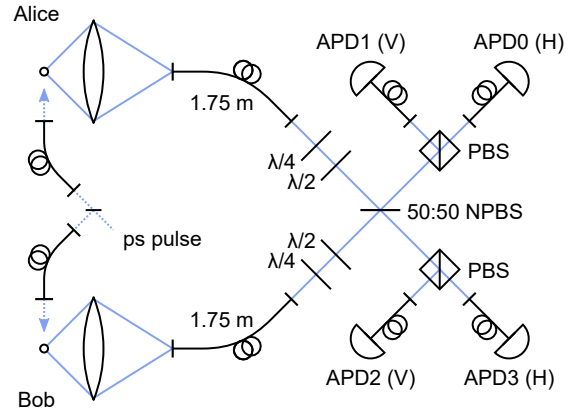


FIG. 3. Overview of apparatus. Single pulses from a frequency-doubled mode-locked laser are split to simultaneously excite ions in Alice and Bob. The spontaneously emitted photons are collected into single-mode fibers, with waveplates directly after the fibers to rotate the polarization. The photons are then directed onto a 50:50 NPBS, and detected on single-mode fiber-coupled APDs following PBSs. To minimize the polarization dependence of the NPBS, we use a small angle of incidence ($\approx 10^\circ$). The same apparatus is used for single-ion/photon experiments.

and are therefore suppressed. The remaining 1.3 % to 1.5 % (system-dependent) error is attributed to ion qubit dephasing during the 60 μs delay between photon detection and tomography, and is expected to be due to excess noise in the applied magnetic field.

To remotely entangle the ion qubits, we erase the path information of photons entangled with each ion and subsequently project the ion-ion state via a destructive measurement on the photon polarizations. A coincidence detection on an appropriate pair of detectors heralds one of two Bell states; $|\Psi_{\text{photon}}^+\rangle := (|\text{VH}\rangle + |\text{HV}\rangle)/\sqrt{2}$ if the detectors are on the same output port of the NPBS, and $|\Psi_{\text{photon}}^-\rangle := (|\text{VH}\rangle - |\text{HV}\rangle)/\sqrt{2}$ if the detectors are on different output ports. Detection of $|\Psi_{\text{photon}}^\pm\rangle$ projects the ions correspondingly into $|\Psi_{\text{ion}}^\pm\rangle := (|\uparrow\downarrow\rangle \pm e^{i\phi} |\downarrow\uparrow\rangle)/\sqrt{2}$, where the phase ϕ is stable [32] and can be transformed to zero with local operations, so is unimportant here.

The probability of successfully heralding an entanglement event is given [17] by

$$P = p_{\text{Bell}} [P_\downarrow P_e P_S P_{\text{click}}]^2, \quad (2)$$

where $p_{\text{Bell}} = 1/2$ because we have valid heralds only for two of the four possible two-photon Bell states, $P_\downarrow \approx 0.99$ is the probability of preparing the correct ground state before excitation, $P_e \approx 0.95$ is the population transferred to the excited state by the pulsed excitation beam, $P_S \approx 0.95$ is the probability of decaying to the $S_{1/2}$ ground states and P_{click} is the probability of detecting a

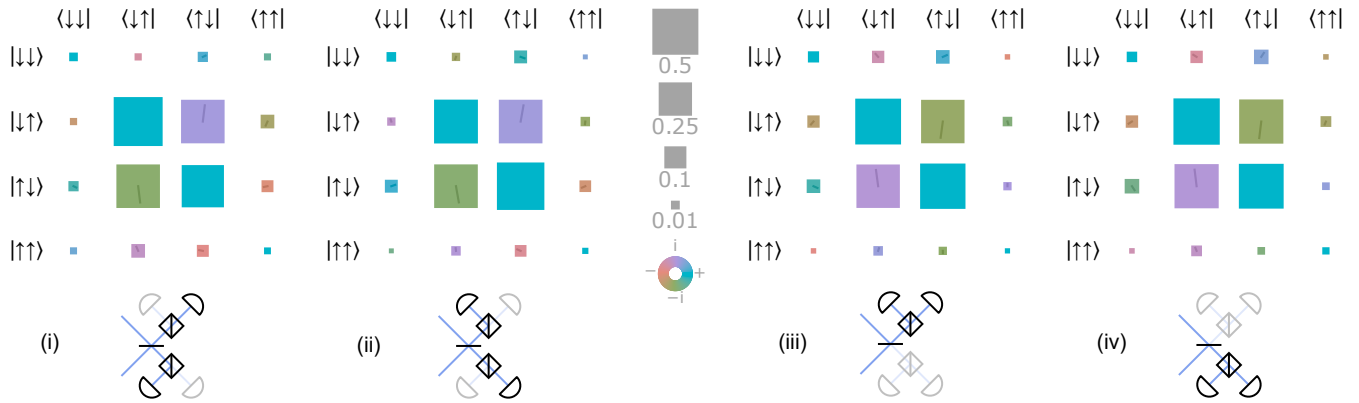


FIG. 4. The remote ion-ion density matrices and corresponding herald patterns (i)-(iv) as per the detector arrangement in Fig. 3. Detector clicks on opposing sides of the 50:50 beamsplitter (i, ii) herald projection into $|\Psi_{\text{ion}}^-\rangle$, while clicks on the same side (iii, iv) herald $|\Psi_{\text{ion}}^+\rangle$. The average fidelity of all four patterns to the nearest maximally entangled state is 94.0(5) %, at a heralded rate of 182 s^{-1} . (In this diagram the area of each square gives the magnitude of the matrix element, with the color representing the complex phase, according to the key shown.)

photon emitted by an ion. We measure $P = 2.18 \times 10^{-4}$; given the average attempt rate (including Doppler cooling) of 833 kHz , this yields a heralded rate of ion-ion entanglement of 182 s^{-1} .

After detection of a two-photon herald, we perform two-qubit tomography to verify the entangled state, using a series of single-qubit rotations and projective measurements [33]. The MLE ion-ion state is calculated for each of the four herald patterns individually, as shown in Fig. 4, indicating an average fidelity of 94.0(5) % to the closest maximally-entangled state [34].

The total ion-ion infidelity is dominated by errors in the ion-photon fidelity from each trap as described above, totalling 4.4 %, which includes errors in the ion-qubit rotations, ion dephasing, and polarization mixing effects. Additional infidelities include: the measured imperfections of the beamsplitters in the Bell state analyzer, $\lesssim 0.17\%$; temporal misalignment of the photons, $\lesssim 0.13\%$; and dark counts, which contribute $\lesssim 0.05\%$ despite a relatively high dark count rate of $\sim 60\text{ s}^{-1}$. The error due to mismatch of the photon modes at the NPBS was not quantified, but is bounded by the measured fidelity to $\lesssim 1.3\%$.

In summary, we have used a new combination of collection geometry and excitation scheme to demonstrate remote entanglement between two atomic ion qubits at much higher rates and fidelities than previously measured. The dominant infidelities arose from single-ion manipulations and coherence time, due to noise in the applied magnetic field and other known technical issues. An order of magnitude of rate improvement is feasible by reducing latencies and the duration of state preparation shown in Fig. 2. Further rate gains could exploit the quadratic dependence on detection efficiency indicated by Eq. 2, by using detectors of higher quantum

efficiency, improving the mode matching into the fibers or using higher numerical aperture lenses to increase collection efficiency. Significantly greater increases could in principle be realized by the use of a mirror close to the ion [35, 36], or via the Purcell enhancement provided by an optical cavity [37–40]. The measured structure of the remote state produced is such that only two entangled pairs would be needed to distill a single remote entangled pair at or above 99 % fidelity [41]. This allows the photonic link to approach the performance of state-of-the-art local operations, enabling a variety of quantum networking applications.

We would like to thank Peter Maunz (Sandia National Laboratories) for supplying HOA2 ion traps, and the developers of ARTIQ [42]. BCN acknowledges funding from the U.K. National Physical Laboratory. CJB acknowledges support from a UKRI FL Fellowship, and is a Director of Oxford Ionics Ltd. This research was supported by the U.K. EPSRC “Networked Quantum Information Technology” Hub and the E.U. AQTION Quantum Flagship project.

* These two authors contributed equally

† Present address: ColdQuanta UK Ltd, Oxford

‡ chris.ballance@physics.ox.ac.uk

- [1] D. P. DiVincenzo, The Physical Implementation of Quantum Computation, *Fortschritte der Physik* **48**, 771 (2000).
- [2] T. P. Harty, D. T. C. Allcock, C. J. Ballance, L. Guidoni, H. A. Janacek, N. M. Linke, D. N. Stacey, and D. M. Lucas, High-Fidelity Preparation, Gates, Memory, and Readout of a Trapped-Ion Quantum Bit, *Physical Review Letters* **113**, 220501 (2014).
- [3] C. J. Ballance, T. P. Harty, N. M. Linke, M. A. Sepiol,

and D. M. Lucas, High-Fidelity Quantum Logic Gates Using Trapped-Ion Hyperfine Qubits, *Physical Review Letters* **117**, 060504 (2016).

[4] J. P. Gaebler, T. R. Tan, Y. Lin, Y. Wan, R. Bowler, A. C. Keith, S. Glancy, K. Coakley, E. Knill, D. Leibfried, and D. J. Wineland, High-Fidelity Universal Gate Set for ${}^9\text{Be}^+$ Ion Qubits, *Physical Review Letters* **117**, 060505 (2016).

[5] Y. Wang, M. Um, J. Zhang, S. An, M. Lyu, J. N. Zhang, L. M. Duan, D. Yum, and K. Kim, Single-qubit quantum memory exceeding ten-minute coherence time, *Nature Photonics* **11**, 646 (2017).

[6] M. A. Sepiol, A. C. Hughes, J. E. Tarlton, D. P. Nadlinger, T. G. Ballance, C. J. Ballance, T. P. Harty, A. M. Steane, J. F. Goodwin, and D. M. Lucas, Probing Qubit Memory Errors at the Part-per-Million Level, *Physical Review Letters* **123**, 110503 (2019).

[7] D. Kielpinski, C. Monroe, and D. J. Wineland, Architecture for a large-scale ion-trap quantum computer, *Nature* **417**, 709 (2002).

[8] C. Monroe and J. Kim, Scaling the Ion Trap Quantum Processor, *Science* **339**, 1164 (2013).

[9] J. Kim, P. Maunz, T. Kim, J. Hussman, R. Noek, A. Mehta, C. Monroe, T. Ralph, and P. K. Lam, Modular Universal Scalable Ion-trap Quantum Computer (MUSIQC), in *AIP Conference Proceedings*, Vol. 1363 (2011) pp. 190–193.

[10] H. M. Meyer, R. Stockill, M. Steiner, C. Le Gall, C. Matthiesen, E. Clarke, A. Ludwig, J. Reichel, M. Atatüre, and M. Köhl, Direct Photonic Coupling of a Semiconductor Quantum Dot and a Trapped Ion, *Physical Review Letters* **114**, 123001 (2015).

[11] H. J. Kimble, The quantum internet, *Nature* **453**, 1023 (2008).

[12] A. Broadbent, J. Fitzsimons, and E. Kashefi, Universal Blind Quantum Computation (2009) pp. 517–526.

[13] V. M. Schäfer, C. J. Ballance, K. Thirumalai, L. J. Stephenson, T. G. Ballance, A. M. Steane, and D. M. Lucas, Fast quantum logic gates with trapped-ion qubits, *Nature* **555**, 75 (2018).

[14] A. Walther, F. Ziesel, T. Ruster, S. T. Dawkins, K. Ott, M. Hettrich, K. Singer, F. Schmidt-Kaler, and U. Poschinger, Controlling Fast Transport of Cold Trapped Ions, *Physical Review Letters* **109**, 080501 (2012).

[15] R. Bowler, J. Gaebler, Y. Lin, T. R. Tan, D. Hanneke, J. D. Jost, J. P. Home, D. Leibfried, and D. J. Wineland, Coherent Diabatic Ion Transport and Separation in a Multizone Trap Array, *Physical Review Letters* **109**, 080502 (2012).

[16] C. Monroe, R. Raussendorf, A. Ruthven, K. R. Brown, P. Maunz, L.-M. Duan, and J. Kim, Large-scale modular quantum-computer architecture with atomic memory and photonic interconnects, *Physical Review A* **89**, 022317 (2014).

[17] D. Hucul, I. V. Inlek, G. Vittorini, C. Crocker, S. Debnath, S. M. Clark, and C. Monroe, Modular entanglement of atomic qubits using photons and phonons, *Nature Physics* **11**, 37 (2015).

[18] S. Ritter, C. Nölleke, C. Hahn, A. Reiserer, A. Neuzner, M. Uphoff, M. Mücke, E. Figueroa, J. Bochmann, and G. Rempe, An elementary quantum network of single atoms in optical cavities, *Nature* **484**, 195 (2012).

[19] P. C. Humphreys, N. Kalb, J. P. J. Morits, R. N. Schouten, R. F. L. Vermeulen, D. J. Twitchen, M. Markham, and R. Hanson, Deterministic delivery of remote entanglement on a quantum network, *Nature* **558**, 268 (2018).

[20] A. Delteil, Z. Sun, W.-b. Gao, E. Togan, S. Faelt, and A. Imamolu, Generation of heralded entanglement between distant hole spins, *Nature Physics* **12**, 218 (2016).

[21] R. Stockill, M. J. Stanley, L. Huthmacher, E. Clarke, M. Hugues, A. J. Miller, C. Matthiesen, C. Le Gall, and M. Atatüre, Phase-Tuned Entangled State Generation between Distant Spin Qubits, *Physical Review Letters* **119**, 010503 (2017).

[22] M. Lettner, M. Mücke, S. Riedl, C. Vo, C. Hahn, S. Baur, J. Bochmann, S. Ritter, S. Dürr, and G. Rempe, Remote Entanglement between a Single Atom and a Bose-Einstein Condensate, *Physical Review Letters* **106**, 210503 (2011).

[23] B. Hensen, H. Bernien, A. E. Dréau, A. Reiserer, N. Kalb, M. S. Blok, J. Ruitenberg, R. F. L. Vermeulen, R. N. Schouten, C. Abellán, W. Amaya, V. Pruneri, M. W. Mitchell, M. Markham, D. J. Twitchen, D. Elkouss, S. Wehner, T. H. Taminiau, and R. Hanson, Loophole-free Bell inequality violation using electron spins separated by 1.3 kilometres, *Nature* **526**, 682 (2015).

[24] M. Żukowski, A. Zeilinger, M. A. Horne, and A. K. Ekert, Event-ready-detectors” Bell experiment via entanglement swapping, *Physical Review Letters* **71**, 4287 (1993).

[25] R. Nigmatullin, C. J. Ballance, N. D. Beaudrap, and S. C. Benjamin, Minimally complex ion traps as modules for quantum communication and computing, *New Journal of Physics* **18**, 103028 (2016).

[26] B. B. Blinov, D. L. Moehring, L. M. Duan, and C. Monroe, Observation of entanglement between a single trapped atom and a single photon, *Nature* **428**, 153 (2004).

[27] D. L. Moehring, P. Maunz, S. Olmschenk, K. C. Younge, D. N. Matsukevich, L.-M. Duan, and C. Monroe, Entanglement of single-atom quantum bits at a distance, *Nature* **449**, 68 (2007).

[28] C. Simon and W. T. M. Irvine, Robust Long-Distance Entanglement and a Loophole-Free Bell Test with Ions and Photons, *Physical Review Letters* **91**, 110405 (2003).

[29] Sandia National Laboratories HOA2.

[30] ARTIQ Sinara hardware, <https://m-labs.hk/experiment-control/sinara-core/>.

[31] Laser Components COUNT BLUE, measured quantum efficiency 65 % at 422 nm.

[32] L. J. Stephenson, *Entanglement between nodes of a quantum network*, Ph.D. Thesis, University of Oxford (2019).

[33] See Supplemental Material.

[34] P. Badzigg, M. Horodecki, P. Horodecki, and R. Horodecki, Local environment can enhance fidelity of quantum teleportation, *Physical Review A* **62**, 012311 (2000).

[35] G. Shu, N. Kurz, M. R. Dietrich, and B. B. Blinov, Efficient fluorescence collection from trapped ions with an integrated spherical mirror, *Physical Review A* **81**, 042321 (2010).

[36] M. Fischer, M. Bader, R. Maiwald, A. Golla, M. Sondermann, and G. Leuchs, Efficient saturation of an ion in free space, *Applied Physics B* **117**, 797 (2014).

[37] J. I. Cirac, P. Zoller, H. J. Kimble, and H. Mabuchi, Quantum State Transfer and Entanglement Distribution

among Distant Nodes in a Quantum Network, *Physical Review Letters* **78**, 3221 (1997).

[38] T. Kim, P. Maunz, and J. Kim, Efficient collection of single photons emitted from a trapped ion into a single-mode fiber for scalable quantum-information processing, *Physical Review A* **84**, 063423 (2011).

[39] A. Stute, B. Casabone, P. Schindler, T. Monz, P. O. Schmidt, B. Brandstätter, T. E. Northup, and R. Blatt, Tunable ionphoton entanglement in an optical cavity, *Nature* **485**, 482 (2012).

[40] A. Stute, B. Casabone, B. Brandstätter, K. Friebe, T. E. Northup, and R. Blatt, Quantum-state transfer from an ion to a photon, *Nature Photonics* **7**, 219 (2013).

[41] Personal communication, Simon Benjamin.

[42] S. Bourdeauducq *et al.*, m-labs/artiq: 4.0 (Version 4.0) (2018).

Supplemental material for ‘High-rate, high-fidelity entanglement of qubits across an elementary quantum network’

L. J. Stephenson,* D. P. Nadlinger,* B. C. Nichol, S. An, P. Drmota,

T. G. Ballance,[†] K. Thirumalai, J. F. Goodwin, D. M. Lucas, and C. J. Ballance[‡]

Department of Physics, University of Oxford, Clarendon Laboratory, Parks Road, Oxford OX1 3PU, U.K.

S1. PHOTON COLLECTION

To collect 422 nm photons emitted by the two ions, custom-designed lens objectives manufactured by Photon Gear [1] are used. They provide near-diffraction-limited performance at an input-side numerical aperture of 0.6 (specified: ≤ 0.08 waves rms at 403.1 nm). The image-side numerical aperture is 0.09, designed to match the ion emission into standard, commercially available step-index fused-silica fibers.

The objective lens is mounted on a five-axis stage for fine control over translational and rotational alignment. After fitting the observed point spread function with a low-order Zernike polynomial model similar to ref. [2], a cylindrical lens is inserted near the image plane to correct for residual aberrations likely caused by varying thickness across the vacuum viewport.

The tip of the collection fiber is mounted on a three-axis positioning stage, which can be adjusted using open-loop piezo actuators to correct for mechanical relaxation and slow, thermal drifts. Automatically tracking the optimum in observed fluorescence count rate allows us to retain good fiber-coupling efficiency over many days. (The short-term passive stability of the system was sufficient for typical experiments, such as the for the data presented in the main text, to be conducted without interruptions for realignment.)

S2. ION-PHOTON TOMOGRAPHY

In the following, we discuss the experiments performed to separately characterize the ion-photon interface of each ion trap node, that is, the quantum state tomography measurements of the joint ion-photon state following picosecond laser excitation.

To implement the necessary measurements on the photonic state, we use the same Bell state analyzer apparatus as for the remote entanglement experiment (see Fig. 3 in the main manuscript), but allow only light from one trap to enter the system. We determine the fast axes and retardances of the individual waveplates separately, and then run the experiment while varying their orientation in a motorized mount, reading out the ion state after a click has been observed on APD0.

We choose to analyze the ion state for all combinations of fast-axis angles of $\{0, \pi/4\}$ for the quarter-wave plate,

and $\{0, \pi/8, \pi/4, 3\pi/8\}$ for the half-wave plate, defined with respect to the measurement polarizer. This implements an over-complete set of projectors for measuring the photonic state. (For ideal waveplates, several of these choices would give rise to the same measurement projector.)

To analyze the ion state, we execute a sequence of 674 nm laser pulses to map part of the population into $|D_{5/2}, m=-3/2\rangle$ and optionally apply extra $\pi/2$ -rotations around an axis in the xy plane. As the phase of the ion-photon state in the laboratory frame is set with the detection of the photon, these analysis sequences are triggered at a fixed time offset from the avalanche photodetector click (with ~ 1 ns precision).

The results from two such tomography runs for Alice and Bob are shown in Fig. S1. In total, 624 000 (572 000) copies of the ion-photon state were measured in Alice (Bob) for these datasets, distributed over 27 min (18 min) of wall clock time. The density matrix estimates are obtained by direct numerical optimization of the likelihood function over the $15 + 1$ real degrees of freedom parameterizing the state and the overall collection efficiency. From those estimates, the fully entangled fraction [3], that is, the fidelity to the nearest maximally entangled state, is computed as 97.90(12) % and 97.70(12) %, respectively, where the errors are given as the s.e.m. obtained from parametric bootstrapping.

We make no attempt to control the polarization rotation introduced by the single-mode fiber linking the ion traps with the polarization state analyzer setup. This results in an extra, a priori unknown, unitary transformation on the photonic part of the observed state. An arbitrary choice of phase reference is also made for the ion’s state. To aid visual interpretation, the same MLE density matrix results are hence shown in Fig. S2 after post-processing with local rotations to maximize their overlap with $|\Phi^+\rangle := (|\downarrow H\rangle + |\uparrow V\rangle)/\sqrt{2}$. Drifts in birefringence due to ambient temperature and mechanical stress lead to slow changes in the unitary induced by the fiber, but we typically observe it to be stable to $\gtrsim 99\%$ in state overlap over many days.

Imperfections in the 674 nm laser pulses and ion qubit decoherence due to magnetic field noise are expected to have a significant effect on the observed ion-photon correlations (see main text). While these effects can be characterized separately, we do not adjust the measurement projectors assumed in the tomography analysis for

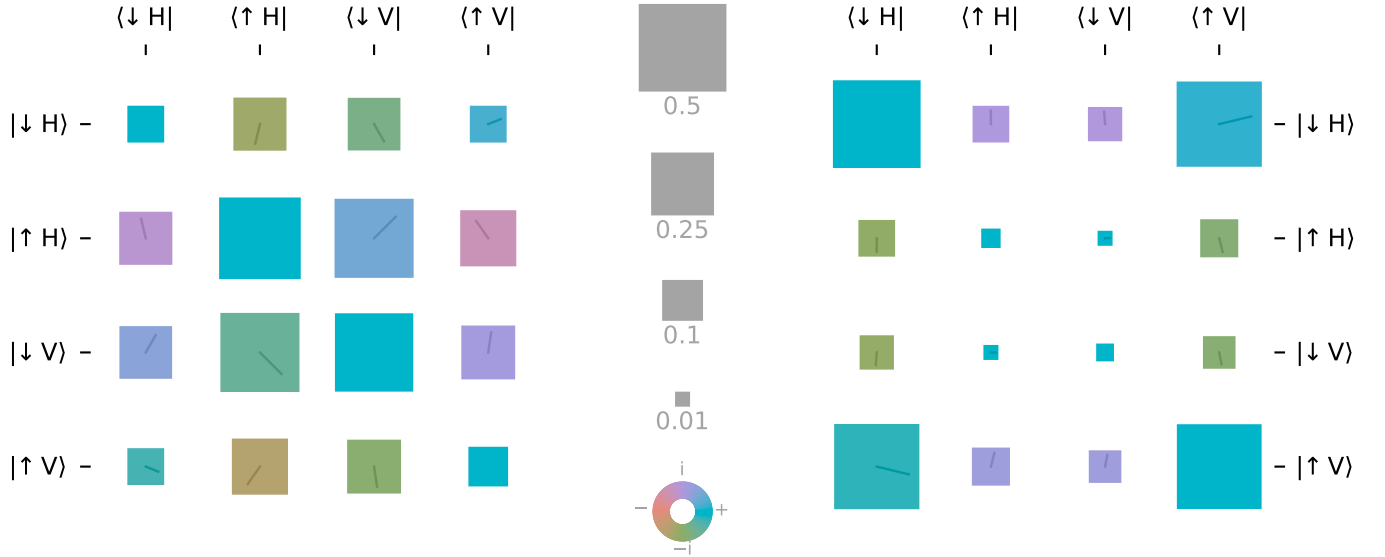


FIG. S1. Maximum-likelihood estimates of the joint ion-photon state produced in nodes Alice (left) and Bob (right), obtained from 624 000 and 572 000 individual state tomography measurements, respectively. The fully entangled fractions are $\mathcal{F}_{\text{Alice}} = 97.90(12)\%$ and $\mathcal{F}_{\text{Bob}} = 97.70(12)\%$, respectively, with the error given as the s.e.m. from parametric bootstrapping.

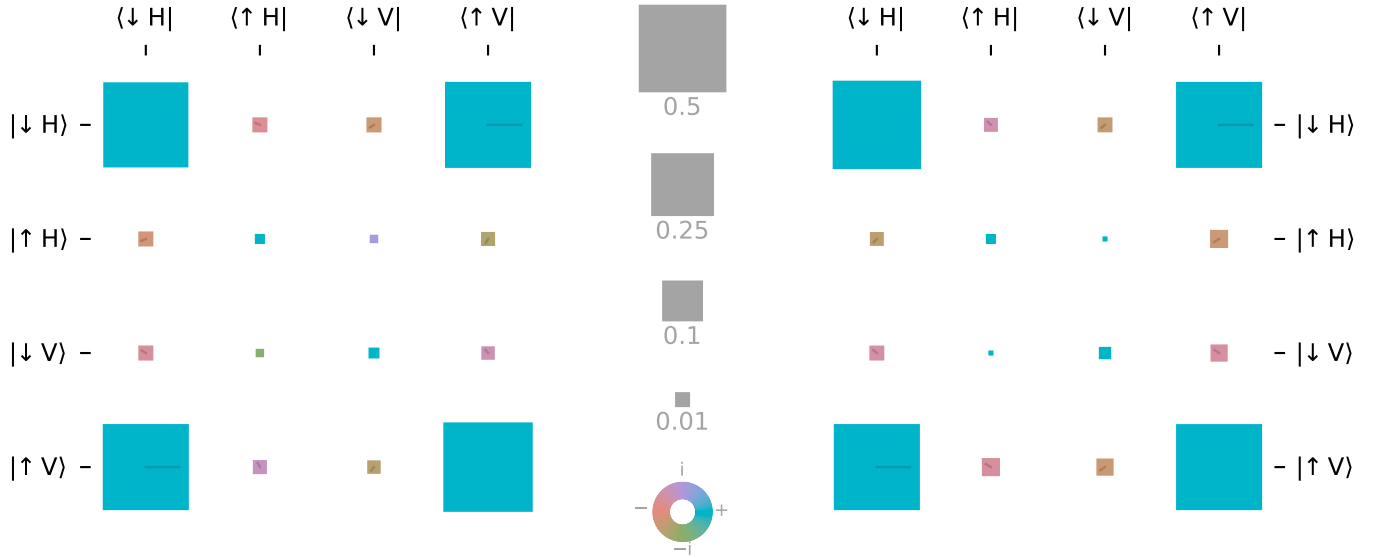


FIG. S2. Maximum-likelihood ion-photon state estimates in nodes Alice (left) and Bob (right) from Fig. S1, transformed post-hoc with unitary operations acting locally on the two subsystems to maximize the overlap with the Bell state $|\Phi^+\rangle := (|\downarrow H\rangle + |\uparrow V\rangle)/\sqrt{2}$.

any such errors (nor for imperfect state discrimination). As such, the tomographic estimate provides only a lower bound for the isolated performance of the ion-photon interface.

S3. ION-ION TOMOGRAPHY

In the main text, we present a performance evaluation of the photonic entanglement generation procedure using tomography of the joint ion-ion quantum state.

To obtain tomography data, we first set the orientation of the waveplate pairs on the input to the Bell state analyzer apparatus to compensate the birefringence of

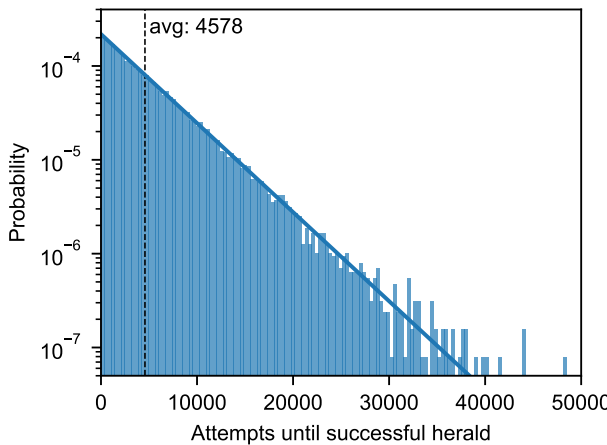


FIG. S3. Histogram of the number of excitation attempts necessary until a two-photon herald event was observed during acquisition of the ion-ion state tomography data presented in the main text. The solid line shows the exponential distribution corresponding to a Poisson process with success probability $1/4578 = 2.18 \times 10^{-4}$. The effective attempt rate is 833 kHz after including the amortized cost of periodic cooling operations, resulting in an average remote entanglement generation rate of 182 s^{-1} .

the fiber-optical links. We do this ahead-of-time in separate experiments by iteratively optimizing the waveplate orientations for each node to maximize the probability of obtaining the ion $|\downarrow\rangle$ state after detecting a photon on APD0. This way, the polarizations incident on the non-polarizing beam splitter for either decay channel are matched. Choosing equal Zeeman qubit frequencies by equalizing the magnetic field strengths then removes any dependence of the resulting state on the photon detection times.

The state of each ion qubit is measured along the x -, y - or z -axis of the Bloch sphere, giving rise to nine possible measurement settings, each corresponding to a projective measurement onto the four eigenvectors of a tensor product of Pauli matrices. For the data presented in the main text, each measurement is performed on 1000 heralded states. For each attempt, we permit all four heralding detector combinations and record which occurred, to later separate them for data analysis [4]. We iterate four times through a random permutation of basis combinations, analyzing a total of 36 000 ion-ion states.

In total, the data acquisition time was approximately 10 min. A total of 165 321 248 entanglement attempts were made, with the individual number of trials until success well-described by an exponential distribution, shown in Fig. S3.

To obtain an estimate for the quantum state of the system conditioned on each of the four detector click pat-

terns, we perform maximum-likelihood state tomography using a diluted fixed point iteration algorithm [5], which we also verify using direct numerical maximization of the likelihood function. The resulting density matrices are in good agreement with the observed correlations; a comparison of observations and model is shown in Fig. S4. (There is a slight imbalance of observation counts between the four click patterns due to small differences in detector efficiencies.)

The quoted figures of merit (fidelity $\mathcal{F} = 0.940(5)$, entanglement of formation $E_F = 0.838(16)$) are computed from the density matrices and averaged over the detector click patterns. To estimate the statistical error, both parametric bootstrapping (simulated experiments from the MLE density matrices) and non-parametric bootstrapping (resampling of the experimental outcomes) are used, and found to give indistinguishable results; quoted as the s.e.m. above and in the main text. The size of the confidence intervals was also verified against a Bayesian model [6], in which a Hilbert–Schmidt uniform prior for the density matrix is assumed and the posterior distribution for each figures of merit is sampled using a Markov-chain Monte-Carlo algorithm (Metropolis–Hastings, using the implementation from ref. [7]).

No attempt was made to correct for the known qubit manipulation and state readout imperfections, which are a consequence of (uncharacteristically large amounts of) technical noise. As such, the quoted fidelities describe the whole-system performance and should be regarded as an upper bound for the link error.

* These two authors contributed equally

† Present address: ColdQuanta UK Ltd, Oxford

‡ chris.ballance@physics.ox.ac.uk

- [1] Photon Gear Inc., Ontario, NY, United States.
- [2] J. D. Wong-Campos, K. G. Johnson, B. Neyenhuis, J. Mizrahi, and C. Monroe, High-resolution adaptive imaging of a single atom, *Nature Photonics* **10**, 606 (2016).
- [3] P. Badzigg, M. Horodecki, P. Horodecki, and R. Horodecki, Local environment can enhance fidelity of quantum teleportation, *Physical Review A* **62**, 012311 (2000).
- [4] This separation is merely to diagnose unexpected differences between the herald patterns; in an application making use of the remotely entangled state, the click pattern dependence would immediately be corrected by inserting additional local phase rotations into the computation as necessary.
- [5] J. Rehek, Z. Hradil, E. Knill, and A. I. Lvovsky, Diluted maximum-likelihood algorithm for quantum tomography, *Physical Review A* **75**, 042108 (2007).
- [6] P. Faist and R. Renner, Practical and Reliable Error Bars in Quantum Tomography, *Physical Review Letters* **117**, 010404 (2016).
- [7] P. Faist, The tomographer project, v5.4 (2018).

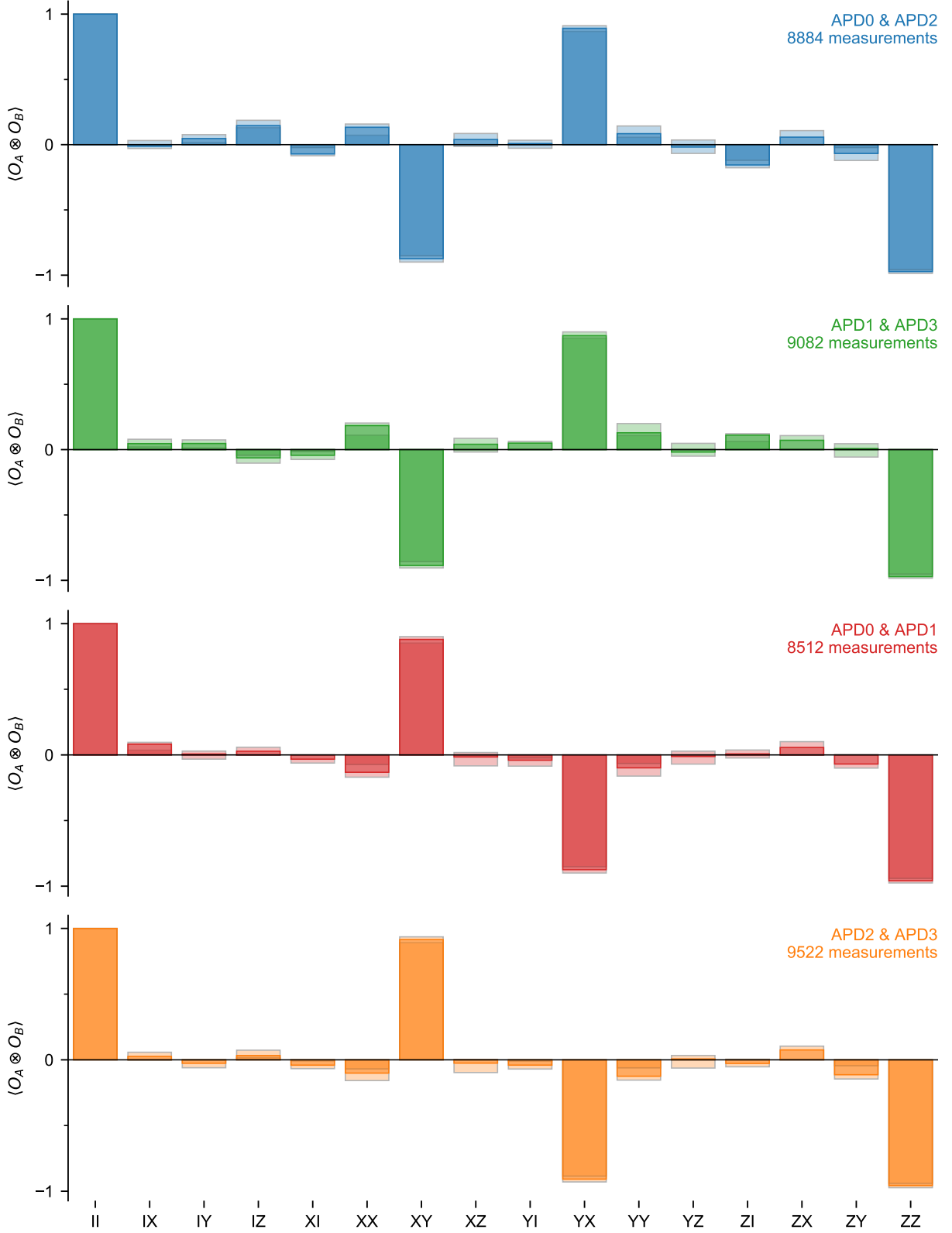


FIG. S4. Ion-ion tomography data for the states heralded by the four different photon detector click patterns (see Fig. 4 in the main text for the resulting density matrices estimates). For each two-qubit Pauli operator, the solid bars show the experimental measurements, whereas transparent bars denote the 95 % confidence interval of the respective expected value from the maximum-likelihood tomography estimate (obtained via bootstrapping).